



Bright lenses are easy to find: spectroscopic confirmation of lensed quasars in the Southern Sky

C. Spinello^{1,2}★ A. Agnello,^{2,3} A. V. Sergeyev,^{4,5} T. Anguita⁶, Ó. Rodríguez^{6,7}, N. R. Napolitano^{1,8} and C. Tortora⁹

¹INAF - Osservatorio Astronomico di Capodimonte, Salita Moiariello, 16, I-80131 Napoli, Italy

²European Southern Observatory, Karl-Schwarzschild-Str 2, D-85748 Garching, Germany

³Dark Cosmology Centre, Juliane Maries Vej 30, 2100 Copenhagen, Denmark

⁴Astronomical Institute of Kharkov National University, 35 Sumskaya St, 61022 Kharkov, Ukraine

⁵Institute of Radio Astronomy of the National Academy of Sciences of Ukraine, 4 Mystetstv St., Kharkiv, 61002, Ukraine

⁶Departamento de Ciencias Fisicas, Universidad Andres Bello Fernandez Concha 700, Las Condes, Santiago, 7550000, Chile

⁷Millennium Institute of Astrophysics, Av. Vicuna Mackenna, 4860 Macul, Santiago, Chile

⁸School of Physics and Astronomy, Sun Yat-sen University Zhuhai Campus, 2 Daxue Road, Tangjia, Zhuhai, Guangdong 519082, P.R. China

⁹INAF - Osservatorio Astrofisico di Arcetri, Largo Enrico Fermi 5, I-50125 Firenze, Italy

Accepted 2018 December 7. Received 2018 December 7; in original form 2018 November 1

ABSTRACT

Gravitationally lensed quasars are valuable, but extremely rare, probes of observational cosmology and extragalactic astrophysics. Progress in these fields has been limited just by the paucity of systems with good ancillary data. Here we present a first spectroscopic confirmation of lenses discovered in the Southern Sky from the DES and KiDS-DR3 footprints. We have targeted seven high-graded candidates, selected with new techniques, with NTT-EFOSC2, and confirmed five of them. We provide source spectroscopic redshifts, image separations, *gri* photometry, and first lens model parameters. The success rate of ~ 70 per cent confirms our forecasts, based on the comparison between the number of candidate doubles and quadruplets in our searches over a $\approx 5000 \text{ deg}^2$ footprint and theoretical predictions.

Key words: gravitational lensing: strong – surveys – Galaxies: formation.

1 INTRODUCTION

When a quasar (QSO) is strongly lensed by a galaxy, it results in multiple images of the same source, possibly accompanied by arcs or rings that map the lensed host galaxy. The light curves of different images are offset by a measurable time delay that depends on cosmological distances to lens and source and the gravitational potential of the lens (Refsdal 1964), which in turn enables one-step measurements of the expansion history of the Universe and the dark-matter haloes of massive lens galaxies at up to $z \sim 0.5$ (e.g. Suyu et al. 2017). The microlensing effect on the multiple QSO images, induced by stars in the deflector, provides a quantitative handle on the stellar content of the lens galaxies (e.g. Schechter & Wambsganss 2002; Bate et al. 2011; Oguri, Rusu & Falco 2014) and, simultaneously, can constrain the inner structure of the source quasar, both accretion disc size and thermal profile (e.g. Anguita et al. 2008; Eigenbrod et al. 2008; Motta et al. 2012) as well as the geometry of the broad-line region (e.g. Sluse et al. 2011; Guerras et al. 2013; Braibant et al. 2014). Finally, source reconstruction of the lensed QSO and its host give a direct view of QSO-host

co-evolution up to $z \sim 2$ (e.g. Peng et al. 2006; Ding et al. 2017). However, lensed quasars are rare on the sky: typically ~ 0.1 per deg^2 at depth and resolution of present-day surveys (Oguri & Marshall 2010, hereafter OM10), since they require a very close alignment of quasars with foreground massive galaxies, or galaxy clusters. The advent of various wide-field surveys, charting extended areas in both hemispheres, helps to overcome the intrinsic rarity of lensed quasars, provided that suitable techniques are devised in order to mine them in massive data bases.

Within our team, we have developed multiple techniques of data mining for lensed quasar searches and recently applied them with success to the Kilo Degree Survey and to the Dark Energy Survey (Agnello & Spinello 2018 and Spinello et al. 2018, hereafter A18 and S18, respectively). We combined different methods to pre-select QSOs, tested their performance and complementarity, and published a list of high-grade candidates, to facilitate (possibly independent) spectroscopic follow-up campaigns.

Here, we present results from the first of these follow-up campaigns, based on data acquired with EFOSC2 (the ESO Faint Object Spectrograph and Camera) mounted at the Nasmyth B focus of the 3.6 m New Technology Telescope (NTT). We give details of the selected candidates in the next section (Section 2). We report on the spectroscopic run in Section 3 and provide photometry and lens

* E-mail: chiara.spinello@gmail.com

model results in Section 4. We finally conclude in Section 5. Whenever needed, we adopt a flat lambda cold dark matter cosmology with $\Omega_\Lambda = 0.7$ and $H_0 = 70 \text{ km s}^{-1} \text{ Mpc}^{-1}$. Magnitudes from DES and KiDS are in the AB system while the ones from WISE are in the Vega system.

2 CANDIDATE SELECTION

We selected our candidates from S18, A18, and from a more recent (hitherto unpublished) list of high-grade candidates found in a similar way. We refer to the two mentioned papers for a detailed description of the morphology- and photometry-based methods that we developed to find lens candidates in wide-sky photometric multiband surveys. The new DES candidates were selected using astrometric offsets of WISE-preselected objects (with the same WISE cuts as in A18) between DES and *Gaia* J2000 coordinates, whereas in A18 we were considering offsets between 2MASS and *Gaia* coordinates. The reason behind this method can be explained by noting that if the deflector and quasar images contribute differently in different bands or in data with different image quality, this should result in centroid offsets of the same object among different surveys. We followed the same procedure as in A18 to detrend such astrometric offsets, and targets were required to have field-corrected offsets between 0.27 and 2.0 arcsec (following tests by S18 and A18).

Targets were then visually inspected via the NCSA-DES access cut-out server¹ to assemble a final list of candidates. Some high-grade candidates were lost at visual inspection, due to visualization issues from large queries in the NCSA web interface (we expected this since A18). As per STRIDES² internal agreements, the full list of lens candidates from DES-versus-*Gaia* offsets will not be disclosed yet.

Some of our candidates have also been found by another group at the same time (Lemon et al. in preparation). Following publication agreements within STRIDES, we give here partially blinded coordinates for two of them. Table 1 reports coordinates and infrared magnitudes (used in the stage of pre-selection) of the systems.

For all the candidates, we perform Direct Image Analysis (DIA), as detailed in S18. Briefly, a PSF model is fit and subsequently subtracted from the survey image to check for the presence of signal from the deflector. In particular, using the PYRAF package³ on the *r*-band images, we simultaneously fit a point-PSF model to the QSO multiple images. We then generated subtracted images which we visually inspect to identify the position of the deflector. For the DES systems, DIA was performed after the spectroscopic run, since we did not use it in A18.

We show the *gri* cut-outs (left-hand panel) and the DIA residuals (right-hand panels) for the candidates reported in A18 and S18 in Fig. 1, and for the new candidates presented in this paper in Fig. 2.

3 SPECTROSCOPIC FOLLOW-UP

Three nights on NTT-EFOSC2 (P0101.A-0298, PI: Anguita) were allocated for follow-up in 2018 July. However, the run was mostly weathered out and we could observe only seven candidates, each with 20 min of integration time. The seeing was stable at $1.0 \pm$

¹<https://des.ncsa.illinois.edu/easyweb>

²STRIDES (strides.astro.ucla.edu) is a broad external collaboration of the DES.

³PYRAF is a product of the Space Telescope Science Institute, which is operated by AURA for NASA.

0.2 arcsec, spectra were reduced using standard (ESO-released) pipelines, and the quasar traces were optimally de-blended using a superposition of Gaussian profiles in the spatial direction (see Morgan et al. 2004; Agnello et al. 2015).

We have confirmed five out of seven lenses, selected from wide-sky photometric surveys, namely DES and KiDS, in the Southern Sky. Concerning the two remaining candidates, KIDS2300-3104 resulted to be a couple of stars, while for bf DES2105-4249 only one trace showed emission lines in its spectrum. This system is therefore not a lensed quasar where the two point-like sources are multiple images of the same object. It is most likely a projection effect of a galaxy + QSOs.

This success rate of ~ 70 per cent is slightly higher but still consistent with the estimates from A18, considering the number of high-graded candidates versus the number of expected lenses over the DES footprint (adopting the lensing rates by OM10).

The NTT spectra of the five confirmed lensed QSOs are shown in Fig. 3, where we also highlight some of the stronger emission lines that enabled the determination of source redshifts, such as CIV $\lambda 1549$, L α , or Mg II $\lambda 2799$. The redshifts were determined with a simultaneous Gaussian fitting to the main emission lines on the spectra of the single components of the quasars, after subtracting the continuum with a fourth-order polynomial function. We note that, although some features deviate from a Gaussian profile, this assumption is sufficient to correctly fit the peak of the lines and measure the redshift of their central wavelength. Once identified the *i*-th emission lines and their rest-frame wavelength ($\lambda_{0,i}$), we defined the peaks of the Gaussians as $\lambda_{0,i}(1+z)$, hence z is a common free parameter for the fitting function, defined as

$$\sum_i A_i e^{\frac{i(\lambda - \lambda_{0,i})(1+z)^2}{2\sigma_i^2}}, \quad (1)$$

where A_i are normalization factors which account for the peak height, and σ_i measure the width of the line. In order to assess the statistical error on the redshift estimates, we have resampled 100 times the spectrum of every source in the fitted range including the three brightest emission-line features. We have randomly re-extracted each pixel value around the current one assuming Gaussian noise given by the rms of the continuum in the regions close to the fitting window. We have then obtained the mean and standard deviation of the best-fitting redshift obtained using a Levenberg–Marquardt method for χ^2 minimization over the 100 resampled spectra. These are reported in Table 2 for all confirmed quasars as final redshift estimates with their statistical uncertainty.

Unfortunately, the faint traces of the lensing galaxies in the spectra did not allow us to securely identify deflector redshifts using the same method. We then estimate photometric redshift distributions using deflector magnitudes from the DES and KIDS multiband images, as explained below.

Using GALFIT (Peng et al. 2002) we performed PSF photometry on all the components (A = brightest QSO image, B = fainter QSO image, G = lens galaxy) for *g*-, *r*-, and *i*-bands. We use a Sefsic profile with $n = 4$ (i.e. we assume a de Vaucouleurs profile) to fit the light distribution of the deflector and point-PSF to fit that of each QSO image. We fit all the components simultaneously. We include the results in Table 2, together with the spectroscopic redshift values for the sources and the photometric redshift values for the deflectors.

To estimate the photometric redshifts of the deflectors we compared their PSF colours as derived above with galaxy spectra from the Sloan Digital Sky Survey (SDSS, DR14, Abolfathi et al. 2018). In particular, for each deflector, we select all galaxies in SpecPhotoAll with colours within 3σ from the ones obtained

Table 1. List of observed candidates with the infrared magnitudes from the WISE catalogue (Wright et al. 2010) that have been used at the pre-selection stage (for some systems, errors of magnitudes are missing from the WISE catalogue). Lenses with partly blinded coordinates have been found independently also by Lemon et al. (in preparation), here indicated as L18.

ID	RA (J2000)	Dec. (J2000)	W1 (mag)	W2 (mag)	W3 (mag)	W4 (mag)	Reference
DES 0247-6349	02:47:54.77	-63:49:23.20	15.10 ± 0.03	14.4 ± 0.04	11.4 ± 0.1	8.6 ± 0.2	A18
DES 2158-5812	21:58:37.30	-58:12:03.90	14.70 ± 0.03	13.9 ± 0.03	11.5 ± 0.2	8.5 ± 0.3	A18
KIDS 2300-3104	23:00:11.82	-31:04:07.07	16.48 ± 0.09	15.7 ± 0.15	11.8	9.1 ± 0.5	S18
KIDS 2307-3039	23:07:18.87	-30:39:15.96	14.88 ± 0.03	14.0 ± 0.04	10.8 ± 0.1	8.2	S18
DES 2105-4249	21:05:04.20	-42:49:36.60	15.59 ± 0.04	14.3 ± 0.05	11.6 ± 0.2	8.4	this paper
DES 01xx-24xx	01:XX:XX.X	-24:XX:XX.X	14.15 ± 0.03	13.17 ± 0.03	10.38 ± 0.08	7.5 ± 0.1	this paper, and L18
DES 03xx-44xx	03:XX:XX.X	-44:XX:XX.X	14.56 ± 0.03	14.2 ± 0.03	12.1 ± 0.2	8.9	this paper, and L18

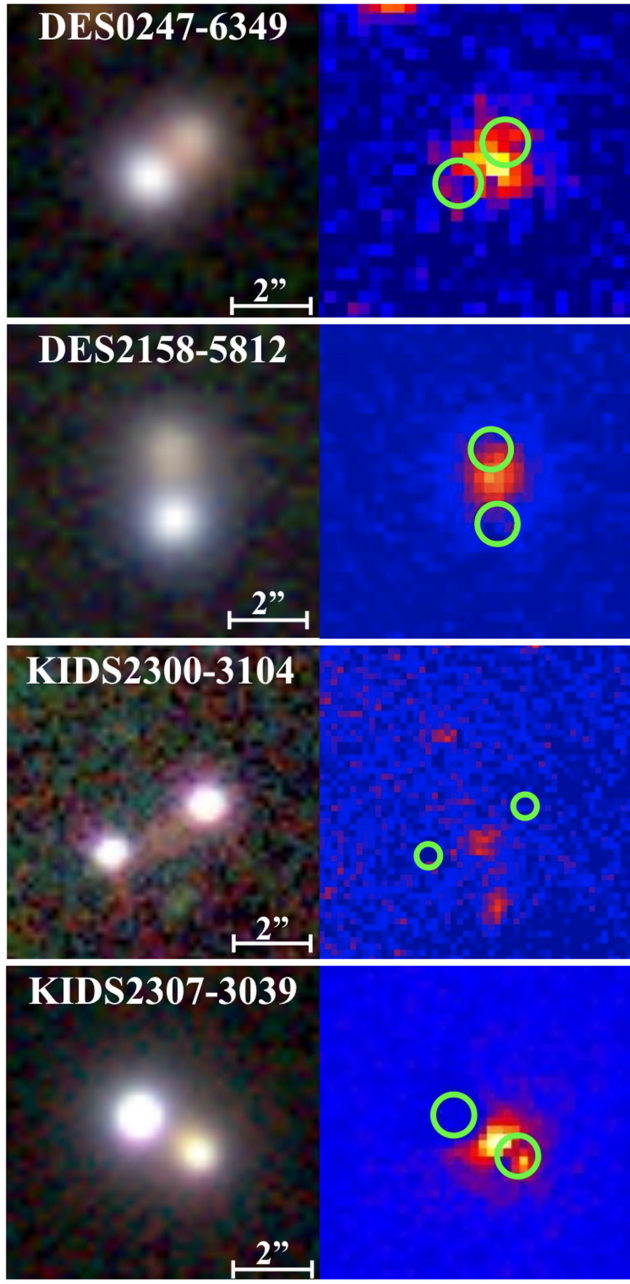


Figure 1. Cut-outs of 7×7 arcsec in size generated combining g -, r -, and i -band images (left-hand panels) and DIA residuals (right-hand panels) for the four candidates from A18 and S18. The cut-outs are modelled as two-point sources plus a galaxy, and the two best-fitting point sources are then subtracted.

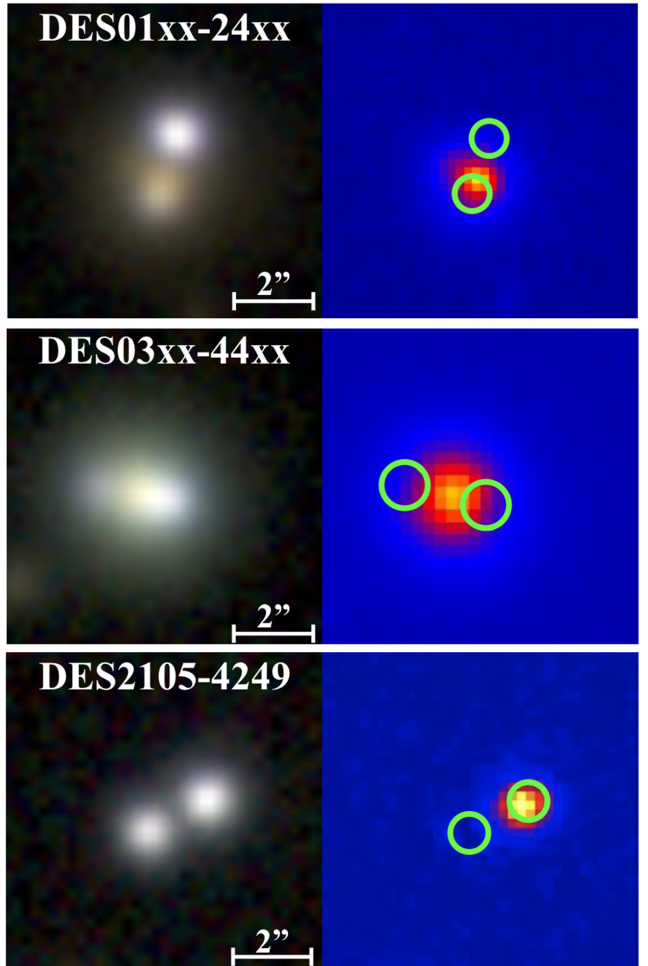


Figure 2. gri cut-outs and DIA residuals (same as in Fig. 1) for the new candidates presented in this paper.

from PSF photometry (we use the `psfMag` and its `psfMagErr` for each band) on the lens and retain their spectroscopic redshifts. Then, we fit a normal distribution to the resulting histograms (plotted in Fig. 4), obtaining the mean and standard deviation of the redshift that we adopted as the fiducial $photo-z$ and its uncertainty.

4 LENS MODELS

We provide here lens model parameters for the confirmed systems. We adopt a Singular Isothermal Sphere with external shear (SIS + XS) described by an Einstein radius R_{Ein} and a shear ampli-

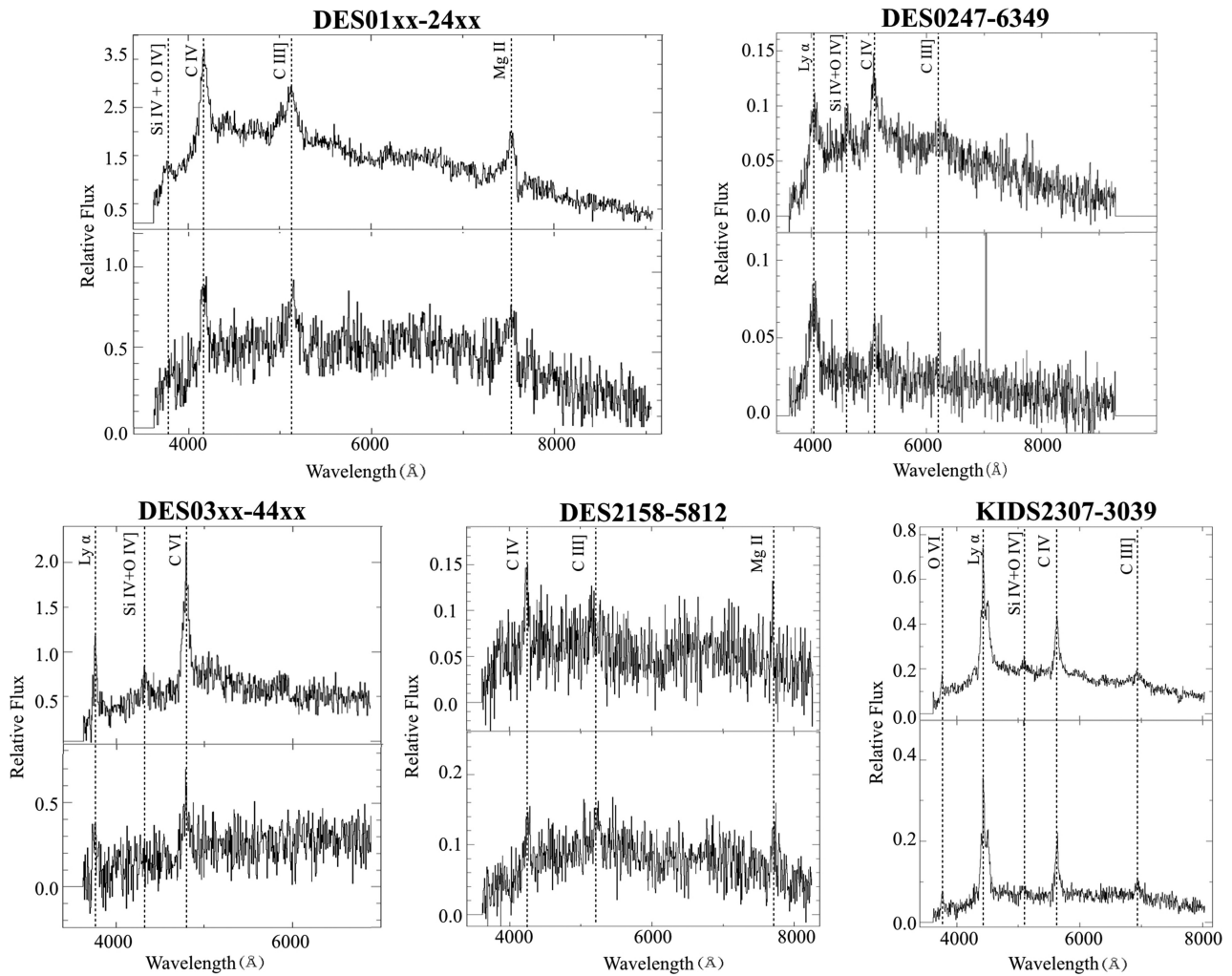


Figure 3. 1D extracted spectra of the two quasar images for the five confirmed new lenses. The most prominent emission lines which allowed us to infer the redshift of the sources are highlighted in the plots. Component A (brighter) is always plotted in the upper panels, while component B (fainter) in the lower ones. The wavelength is always plotted in the observed frame.

Table 2. Astrometric properties of all the components of the five confirmed lenses. Relative positions are given in arcsec and always using as reference the brightest QSOs image (A). Magnitudes in the *gri* bands have been computed performing PSF photometry, using GALFIT (see Section 3).

ID	Comp.	δx (arcsec)	δy (arcsec)	z (redshift)	g (mag)	r (mag)	i (mag)
DES01xx-24xx	A	0.000 ± 0.003	0.000 ± 0.003	1.692 ± 0.001	18.83 ± 0.01	18.87 ± 0.01	18.62 ± 0.01
DES01xx-24xx	B	-0.523 ± 0.013	-1.770 ± 0.013	1.690 ± 0.002	20.49 ± 0.02	20.25 ± 0.05	19.91 ± 0.07
DES01xx-24xx	G	-0.434 ± 0.024	-1.283 ± 0.037	0.22 ± 0.03	20.30 ± 0.04	18.87 ± 0.03	18.31 ± 0.02
DES247-6349	A	0.0 ± 0.003	0.0 ± 0.005	2.303 ± 0.009	19.95 ± 0.01	19.80 ± 0.02	19.81 ± 0.03
DES247-6349	B	$+1.055 \pm 0.013$	0.984 ± 0.013	2.31 ± 0.02	21.13 ± 0.02	20.87 ± 0.06	20.45 ± 0.09
DES247-6349	G	$+0.76 \pm 0.19$	0.60 ± 0.16	0.43 ± 0.08	22.21 ± 0.23	21.11 ± 0.17	19.87 ± 0.13
DES03xx-44xx	A	0.000 ± 0.008	0.000 ± 0.011	2.094 ± 0.001	19.91 ± 0.02	19.88 ± 0.03	19.56 ± 0.02
DES03xx-44xx	B	-1.89 ± 0.03	0.44 ± 0.03	2.093 ± 0.003	21.06 ± 0.02	21.05 ± 0.05	20.64 ± 0.03
DES03xx-44xx	G	-0.742 ± 0.011	0.179 ± 0.005	0.11 ± 0.03	19.08 ± 0.01	18.11 ± 0.01	17.70 ± 0.01
DES2158-5812	A	0.000 ± 0.005	0.000 ± 0.005	1.756 ± 0.004	20.00 ± 0.01	19.92 ± 0.01	19.71 ± 0.01
DES2158-5812	B	-0.124 ± 0.016	1.888 ± 0.018	1.74 ± 0.02	21.71 ± 0.01	21.26 ± 0.10	21.09 ± 0.18
DES2158-5812	G	-0.03 ± 0.04	1.29 ± 0.07	0.41 ± 0.08	21.65 ± 0.14	20.53 ± 0.05	19.64 ± 0.08
KIDS2307-3039	A	0.000 ± 0.008	0.000 ± 0.008	2.640 ± 0.005	18.64 ± 0.02	18.49 ± 0.02	18.57 ± 0.04
KIDS2307-3039	B	-2.046 ± 0.013	-1.291 ± 0.016	2.641 ± 0.003	20.01 ± 0.04	19.78 ± 0.04	19.18 ± 0.07
KIDS2307-3039	G	-1.56 ± 0.13	-0.90 ± 0.13	0.46 ± 0.06	21.6 ± 0.3	20.97 ± 0.11	19.85 ± 0.07

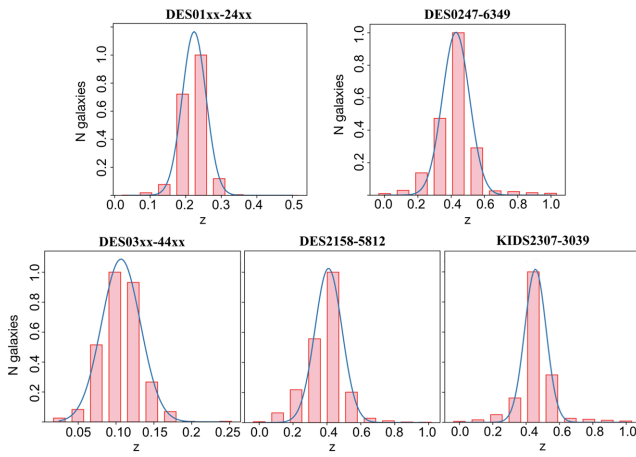


Figure 4. Inference on the photometric redshifts of the deflectors in this sample, using spectroscopic redshifts from SDSS-DR14 SpecPhotoAll galaxies with similar PSF colours (within 3σ uncertainties). The number of galaxies plotted on the y-axis for each system has been normalized to the histogram maximum value.

Table 3. Best-fitting SIS + XS model parameters of the confirmed lenses.

ID	R_{Ein} (arcsec)	M_{Ein} ($10^{11} M_{\odot}$)	γ	μ^a (mag)	Δt^b (d)
DES 01xx-24xx	0.97	1.04	0.06	-1.30	25 ± 4
DES 0247-6349	0.72	1.05	0.04	-0.73	23 ± 6
DES 03xx-44xx	0.96	5.12	0.01	-0.61	-6 ± 2
DES 2158-5812	0.80	1.32	0.16	-2.35	43 ± 13
KIDS 2307-3039	1.19	2.96	0.04	-0.60	99 ± 17

Notes: *a*: model magnitude difference between A and B images

b: the errors are propagated from the shear direction uncertainties and are proportional to $1 \pm \gamma$

tude γ and orientation. The models are fit to the relative astrometry of quasar images and deflectors from above. The errors are propagated from the shear direction and are proportional to $1 \pm \gamma$. The resulting Einstein radii are approximately half the image separations (within ≈ 10 per cent), but the SIS + XS model allows us to account for degeneracies between monopole and quadrupole contributions to the mass. The resulting best-fitting parameters are given in Table 3, where we also give the predicted magnitude differences and time delays. The main contribution of the time-delay uncertainties comes from the photometric redshift estimation. The model magnitude differences are in perfect agreement with the measured magnitude difference in *i*-band reported in Table 2 for DES01xx-24xx, DES0247-6349, and KIDS2307-3039. For the remaining two systems, in one case the difference is underestimated by the model (DES03xx-44xx) and in the other case (DES2158-5812) it is overestimated by it. However, we note that multiple factors might affect the actual flux ratios of lensed quasars: the combination of time delays and source variability, microlensing, substructures, and differential dust reddening in the lens plane. Given that generally the B images show the most chromatic variation (redder than the brightest images), extinction probably plays a major role. Only deeper spectra and deeper photometry would enable quantitative studies of the objects (e.g. Yonehara et al. 1998; Agnello et al. 2017).

Finally, we calculated the total projected mass within the Einstein radius, using the classical lens equation formula (see e.g. Schneider,

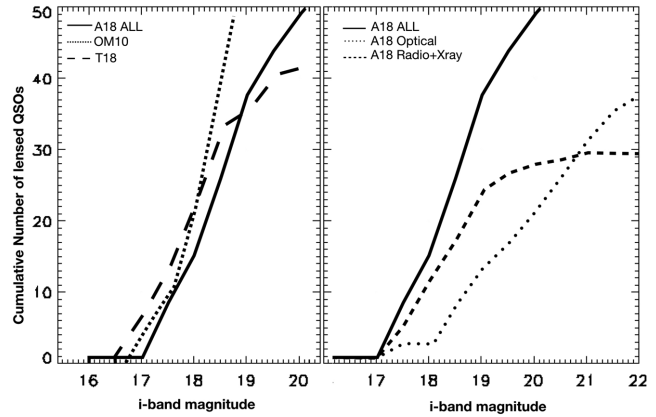


Figure 5. *Left-hand panel:* Cumulative number of targets in bins of *i*-band magnitudes from A18 (solid lines) and scaled for the 70 per cent successful rate obtained here. The comparison with the distribution of targets in DES (dashed line) calculated by the STRIDES Collaboration (Treu et al. 2018) and with predictions from OM10 (dotted line) shows a very good agreement. *Right-hand panel:* Same as in the left-hand panels, but the different lines show candidates selected in A18 from optical bands versus candidates selected from other wavelengths. Selecting QSOs from radio or X-Ray allows us to find fainter lenses.

Ehlers & Falco 1992)

$$M_{\text{Ein}} = R_{\text{Ein}}^2 \frac{c^2 D_l D_s}{4 G D_{ls}}, \quad (2)$$

where D_l is the distance of the lens from the observer, D_s is the distance of the source from the observer, and D_{ls} is the relative distance between the lens and the source. We include the masses in Table 3.

5 DISCUSSION AND FUTURE PROSPECTS

We have presented a sample of previously unknown lenses, found in the Southern hemisphere through new techniques relying on astrometric offsets, and spectroscopically confirmed. The success rate of 5/7 meets the expectations from A18 and S18. The range of source redshifts and Einstein radii is consistent with OM10 predictions, further suggesting that these searches are complete within the photometric completeness of *Gaia*.

Compared to the depth of DES and KiDS, these objects are still at the bright end. This fact has been noted for various independent searches (see Treu et al. 2018, for forecasts on the DES); a large fraction of lenses with faint quasar sources is hitherto undiscovered, and different strategies of target and candidate selection are needed.⁴ This is shown in Fig. 5, where the cumulative distributions of predicted candidate and confirmed lenses are shown. On the left-hand panel, we show the distribution of targets in DES (dashed line) calculated by the STRIDES Collaboration (Treu et al. 2018) and the predictions from OM10 (dotted line). We compare these distributions with the ones of the A18 candidates, rescaled by 0.7 to account for the success rate of this campaign, finding a very good agreement. Moreover, we note that samples relying on optical selection through *Gaia*, such as the one presented in Treu et al. (2018), saturate between $i \approx 18.5$ and $i \approx 20.0$ whereas samples including

⁴See e.g. A18 for the discussion of radio and X-ray searches for lensed quasars over the DES footprint.

radio and X-ray preselection (such as A18) extend to fainter magnitudes and follow the OM10 predictions more closely. The last point appears even more clearly in the right-hand panel of Fig. 5 where we split the A18 candidates according to the preselection method. Below $i \approx 20.5$ the number of lens candidates found through radio and X-rays is larger than the number of systems selected in the optical.

The brightness of most confirmed lenses also means that spectroscopic follow-up, to measure the kinematics of the deflectors, is affordable with current-generation facilities. Through monitoring with nightly-cadence, an accuracy of 5 per cent should be attainable on the time delay (Δt) between quasar light curves in systems with $\Delta t \gtrsim 25$ d (Courbin, private communication). Moreover, if the deflector's velocity dispersion σ is measured, the combination $c^3 \Delta t / \sigma^2 \propto D_l$ of time delay and kinematics would make these systems standard rulers at $z = 0.2\text{--}0.65$, to within ≈ 20 per cent uncertainties (Jee, Komatsu & Suyu 2015; Shajib, Treu & Agnello 2018). For lenses with lower deflector redshift, the time-delay distance $D_{\Delta t} = D_l D_s / ((1 + z_l) D_{ls})$ is proportional to D_l with a factor that is only weakly dependent on cosmological parameters (Ω_Λ , Ω_m). Securing spectroscopic redshifts of the deflectors and measuring time delays would then yield two angular diameter distances per lens.

ACKNOWLEDGEMENTS

The authors wish to thank the anonymous referee for interesting and constructive comments that helped in improving the quality and clarity of the paper.

CS and NRN have received funding from the European Union's Horizon 2020 research and innovation programme under the Marie Skłodowska-Curie actions grant agreement No 664931 and No 721463 to the SUNDIAL ITN network, respectively. TA and OR acknowledge support by the Ministry for the Economy, Development and Tourism's Programa Iniciativa Científica Milenio through grant IC120009, awarded to The Millennium Institute of Astrophysics (MAS). CT acknowledges funding from the INAF PRIN-SKA 2017 program No 1.05.01.88.04.

REFERENCES

- Abolfathi B. et al., 2018, *ApJS*, 235, 42
- Agnello A. et al., 2017, *MNRAS*, 472, 4038
- Agnello A., Spinelli C., 2018 preprint ([arXiv.1805.11103](https://arxiv.org/abs/1805.11103)) (A18)
- Agnello A. et al., 2015, *MNRAS*, 454, 1260
- Anguita T., Schmidt R. W., Turner E. L., Wambsganss J., Webster R. L., Loomis K. A., Long D., McMillan R., 2008, *A&A*, 480, 327
- Bate N. F., Floyd D. J. E., Webster R. L., Wyithe J. S. B., 2011, *ApJ*, 731, 71
- Braibant L., Hutsemékers D., Sluse D., Anguita T., García-Vergara C. J., 2014, *A&A*, 565, L11
- Ding X. et al., 2017, *MNRAS*, 465, 4634
- Eigenbrod A., Courbin F., Meylan G., Agol E., Anguita T., Schmidt R. W., Wambsganss J., 2008, *A&A*, 490, 933
- Guerreras E., Mediavilla E., Jimenez-Vicente J., Kochanek C. S., Muñoz J. A., Falco E., Motta V., Rojas K., 2013, *ApJ*, 778, 123
- Jee I., Komatsu E., Suyu S. H., 2015, *J. Cosmol. Astropart. Phys.*, 11, 033
- Morgan N. D., Caldwell J. A. R., Schechter P. L., Dressler A., Egami E., Rix H.-W., 2004, *AJ*, 127, 2617
- Motta V., Mediavilla E., Falco E., Muñoz J. A., 2012, *ApJ*, 755, 82
- Oguri M., Marshall P. J., 2010, *MNRAS*, 405, 2579
- Oguri M., Rusu C. E., Falco E. E., 2014, *MNRAS*, 439, 2494
- Peng C. Y., Ho L. C., Impey C. D., Rix H.-W., 2002, *AJ*, 124, 266
- Peng C. Y., Impey C. D., Rix H.-W., Kochanek C. S., Keeton C. R., Falco E. E., Lehár J., McLeod B. A., 2006, *ApJ*, 649, 616
- Refsdal S., 1964, *MNRAS*, 128, 307
- Schechter P. L., Wambsganss J., 2002, *ApJ*, 580, 685
- Schneider P., Ehlers J., Falco E. E., 1992, *Astronomy and Astrophysics Library*. Springer-Verlag, Berlin Heidelberg, New Yourk, p. 112
- Shajib A. J., Treu T., Agnello A., 2018, *MNRAS*, 473, 210
- Sluse D. et al., 2011, *A&A*, 528, A100
- Spinelli C. et al., 2018, *MNRAS*, 480, 1163
- Suyu S. H. et al., 2017, *MNRAS*, 468, 2590
- Treu T. et al., 2018, *MNRAS*, 481, 1041
- Wright E. L. et al., 2010, *AJ*, 140, 1868
- Yonehara A., Mineshige S., Mamoto T., Fukue J., Umemura M., Turner E. L., 1998, *ApJ*, 501, L41

This paper has been typeset from a TeX/LaTeX file prepared by the author.